Closed Cross-Section Dual-Matrix Composite Hinge for Deployable Structures

Maria Sakovsky[1], Sergio Pellegrino

Graduate Aerospace Laboratories, California Institute of Technology, 1200 E. California Blvd., Pasadena, CA, USA, 91125

Abstract

Dual-matrix composite structures with localized elastomer composite hinges have been proposed to enable packaging with much smaller fold radii than allowed by traditional resin-based fiber reinforced composites. Previous studies have been limited to proof-of-concept of folding capabilities and constitutive modeling of elastomer composites. A novel closed cross-section dual-matrix deployable hinge is studied here to develop the tools for studying the deployment of general dual-matrix structures. A set of tools for the analysis of deployment of this simple structure is developed: an analytic model that minimizes the strain energy in the folded configuration, experimental characterization, and finite element techniques using the LS-Dyna commercial software. The three models are used to predict the packaged shape and deployment moments, and are shown to be in good agreement amongst themselves. The analytic model is used to demonstrate control of the folded shape of the hinge using the stiffness of the elastomer composite. This behavior is verified using finite element models developed in the LS-Dyna commercial code. The simulations are used to predict the localized fold radius of the hinge within 3% and deployment moments within 5% by accounting for the microbuckled stiffness of the elastomer composite.

Keywords: Deployable structures, Space structures, Elastomer composites

---

1. Introduction

Future spacecraft antennas, solar arrays, and telescopes will require deployable structures with high packaging ratios to fit into the fairing of launch vehicles. Previous solutions have used assemblies of rigid rods with mechanical hinges, as in the Astromesh reflector [1], commercial-off-the-shelf deployable solar panels including those from Clyde Space [2], and the James Webb space telescope [3]. These hinges are driven by motors or are spring loaded, resulting in high precision yet heavy and mechanically complex structures. A simpler, alternative approach uses high-strain thin-shell structures which achieve deployment by releasing elastic strain energy stored during packaging. These structures have relatively low mass and can attain high packaging ratios, but can only meet less stringent requirements on deployment precision. The fold radii of high-strain elements are constrained by the elastic limits of their constituent materials, to

---

[1] Corresponding author, email address: `msakovsk@alumni.caltech.edu`

ensure that no permanent damage occurs during folding. Examples of such structures include various types of booms to deploy and support satellite payloads, such as the storable tubular extensible member (STEM) boom [4, 5], the triangular rollable and collapsible (TRAC) boom [6], and the coillable tubular mast (CTM) [7, 8]. Initially these booms were made of metal but more recently they have been fabricated using composite materials.

A newer development is the use of composite materials with an elastomer matrix to allow higher elastic strain limits and hence smaller fold radii in the packaged configuration. This approach is exemplified by the SMART deployable antenna made of a carbon fiber reinforced silicone [9], and the application of elastomer composites to morphing wings [10]. In such structures, an external rigid frame may be required to achieve the desired deployed stiffness and dimensional stability.

Dual-matrix composite shells have been proposed by Caltech and L'Garde as a means of improving the stiffness of elastomer composite structures [11]. Dual-matrix composites consist of a continuous fiber reinforcement impregnated with an elastomer matrix in localized hinge regions and a stiff epoxy matrix elsewhere. These shells are packaged by folding along the hinges and have been used to fold flat sheets with creases forming a Miura-Ori pattern [11], a complex origami crane [12], and conical antenna structures [13].

Previous research on dual-matrix composites has focused on material characterization, especially of the elastomer composites. Francis et al. [14] showed that elastomer composites can be folded elastically to high strains with hinge fold angles as high as 180^o because fiber microbuckling on the compression side of the fold has the effect of decreasing the strain in the fibers. Murphy et al. [15] have studied the elastic strain limits of elastomer composite. Maqueda et al. [11, 16] have examined techniques for predicting homogenized properties of elastomer composites, characterized them experimentally, and studied in detail their microstructure. Lopez-Jimenez et al. [17] have characterized damage in elastomer composites, in particular due to fiber-matrix debonding.

In this paper, a novel dual-matrix composite hinge is used to study the behavior of these materials in a deployable structure. The hinge under study is a short epoxy composite cylindrical shell with two diametrically opposite, length-wise elastomer composite strips that allow, through the formation of localized folds, transverse flattening and longitudinal folding of the cylinder. This study examines the quasi-static deployment behavior of the proposed dual-matrix hinge to demonstrate that dual-matrix composites can be used as deployable structures and to enable design of deployment mechanisms. The study will allow the analysis of more complex structures such as booms, truss frames, and antenna structures as proposed in [13]. In particular, the analysis enables the design of deployment mechanisms for dual-matrix composites by developing the tools to predict the deployment moments and folded shapes.

The paper is organized as follows. Section 2 describes the geometry of the hinge, its fabrication, and material properties. Section 3 presents a characterization of the hinge's deployment mechanics using an analytic model and experimental measurements. Section 4 describes finite element techniques for a deployment model of the hinge in the LS-Dyna commercial software. Section 5 discusses the finite element model results as compared to analytic and experimental characterization. Section 6 concludes the paper.

2. Dual-Matrix Hinge

2.1. Hinge Geometry

A schematic of the hinge is shown in Figure 1. The hinge is composed of a cylindrical fiber reinforced polymer composite tube of diameter, D, and length, L, with two diametrically opposite elastomer composite strips of width, h_c, along the length. The hinge can be folded by means of a single fold with an angle, θ, as illustrated in Figure 1B. Slots of length, w_s, are introduced into the elastomer composite strips to alleviate stresses in the fold region where high changes of Gaussian curvature are introduced in the small region where the longitudinal folds meet with the transverse fold.

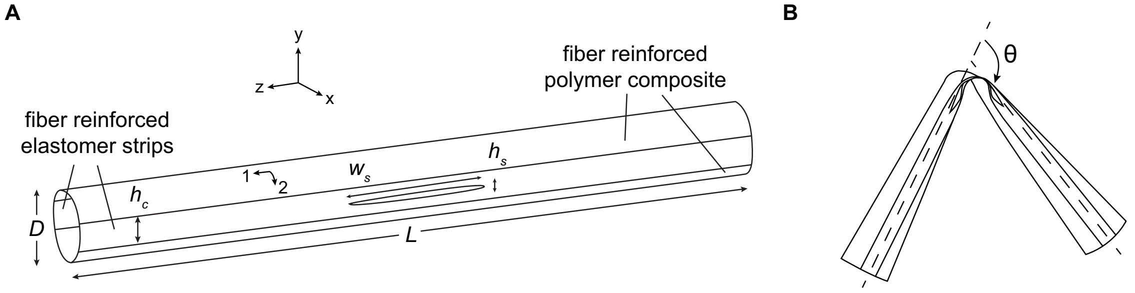

Figure 1: Geometry of dual-matrix hinges (A) definition of hinge geometric parameters (B) illustration of hinge folding.

2.2. Hinge Prototypes

The geometry of the particular hinge prototypes that were built in this study is summarized in Table 1. The hinges were fabricated from dry Astroquartz II (AQ) plain-weave fabric reinforcement (style 525 from JPS Composites [18]) with a UV-cure silicone (LOCTITE 5055 [19]) for the elastomer strips and an epoxy matrix (PMT-F4B from Patz Materials and Technologies [20]) elsewhere. The hinges have a 3-ply quasi-isotropic layup of $[45/0/45]_{pw}$, where the pw subscript indicates that each ply is a plain-weave fabric. A woven reinforcement was selected for the prototypes to ease handling of the dry fibers and to limit fiber-matrix debonding due to loads transverse to the fibers [17]. Tables 2 and 3 summarize the constituent material properties.

	L	D	h_c	h_s	w_s
Value	250	25.4	8	2	0, 10, 40, 50

Table 1: Values for hinge geometric parameters, units are mm.

The fabrication process of the hinge prototypes is illustrated in Figure 2. The hinge was fabricated starting with dry AQ fabric using a wet layup process. The epoxy resin was transferred to the fabric by

Astroquartz II Fibers	
Modulus, E_f (GPa)	72
Poisson's Ratio, ν_f	0.16
Tensile Strength (GPa)	6.0
Density, ρ_f (g/cm^3)	2.2
Fiber Diameter, D_f (μm)	9.0
Style 525 Fabric	
Areal Density (g/m^2)	68
Warp Count (fibers per in.)	50
Fill Count (fibers per in.)	50

Table 2: Material properties of Astroquartz II fibers and style 525 fabric [18].

	Epoxy	Silicone
Modulus, E_m (GPa)	3.39	0.004
Tensile Strength (MPa)	65.5	9.3
Density, ρ_m (g/cm^3)	1.23	0.98
Poisson's Ratio, ν_m	0.35	0.48

Table 3: Material properties of F4-B epoxy [20] and LOCTITE 5055 silicone [19].

applying heat using an electric iron while the silicone strip regions were masked with Kapton. The plies were stacked and the silicone was transferred to the fabric by injecting small amounts with a syringe in the previously masked regions and allowing the silicone to flow until the fabric is fully impregnated. The layup was debulked under vacuum for 30 mins to evacuate any air bubbles from the silicone and to consolidate the layup. This ensured a good cure of the silicone as its cure is inhibited in the presence of oxygen. The silicone was cured between two acrylic plates under a UV lamp (Spectroline UV Lamp XX-15A operating at 365 nm) with an irradiance of 40 mW/cm^2, held at a distance of 35 mm. The layup was wrapped around a cylindrical mold and vacuum bagged. Heat-shrink tubing was applied to the layup underneath the vacuum bagging to prevent wrinkles from printing through to the composite. The epoxy was cured in a standard autoclave cure at 120°C for 2 hours. The slots were cut into the cured hinges using a rotary tool. Figure 3 shows the fabricated prototypes.

The silicone undergoes a condensation cure, producing water and methanol as byproducts which diffuse out of the composite over time. A heat-treatment of 48 hrs at 140°C under vacuum was found to be sufficient to bake-out these byproducts and stabilize the mass of the composite.

Figure 2: Fabrication process of dual-matrix hinge (A) dry AQ plies (B) application of epoxy resin with silicone regions masked (C) application of silicone (D) layup debulking (E) UV-curing of silicone resin (F) layup wrapped around cylindrical mold (G) application of heat-shrink around layup (H) autoclave cure of epoxy resin.

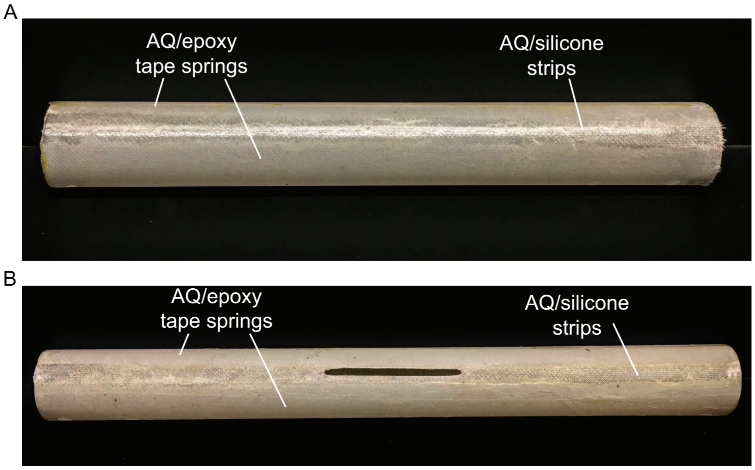

Figure 3: Fabricated dual-matrix hinges (A) hinge with no slot (w_s = 0 mm) (B) hinge with a w_s = 50 mm slot.

2.3. Material Characterization

Accurate values of the composite thickness and fiber volume fractions are required for good estimates of the stiffness of the composites. These were obtained from optical micrographs. Figures 4A and B show micrographs of flat test coupons of the AQ/epoxy and AQ/silicone composites, respectively. The average thicknesses of the two composites were 190 μm and 267 μm. The silicone composite is thicker as less pressure was applied during the cure. At high bending curvatures, the silicone composite undergoes fiber microbuckling on the compression side of the fold, locally increasing the material thickness to 570 μm. The areal densities of the two composites were 0.033 g/mm^2 and 0.037 g/mm^2. The fiber volume fractions of the two composites were 54% and 40%.

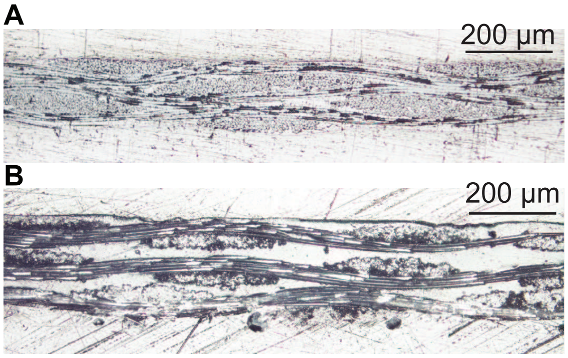

Figure 4: Micrographs of constituent composites (A) AQ/epoxy (B) AQ/silicone.

The deployment of dual-matrix composites is driven by the strain energy stored upon folding of the structure. Hence, an accurate constitutive model for the composites used is required for predicting deployment moments of the hinge. The model considered is a linear elastic laminated plate model with the force and moment resultants given by [21],

$$\begin{bmatrix} \boldsymbol{N} \\ \boldsymbol{M} \end{bmatrix} = \begin{bmatrix} \boldsymbol{A} & \boldsymbol{B} \\ \boldsymbol{B} & \boldsymbol{D} \end{bmatrix} \begin{bmatrix} \boldsymbol{\varepsilon} \\ \boldsymbol{\kappa} \end{bmatrix} \tag{1}$$

where $\boldsymbol{N}$ and $\boldsymbol{M}$ are the force and moment per unit width of the composite plate, respectively, $\boldsymbol{A}$ is the in-plane stiffness, $\boldsymbol{B}$ is the stretching-bending coupling, $\boldsymbol{D}$ is the out-of-plane stiffness, and $\boldsymbol{\varepsilon}$ and $\boldsymbol{\kappa}$ are the mid-plane strains and curvatures, respectively. The stiffness matrices of the composite laminates are computed using Classical Lamination Theory (CLT) as follows,

$$\boldsymbol{A} = \sum_{i=1}^{n} \bar{\boldsymbol{Q}}_{\boldsymbol{i}}(z_{i+1} - z_i) \tag{2}$$

$$\boldsymbol{B} = \frac{1}{2}\sum_{i=1}^{n} \bar{\boldsymbol{Q}}_{\boldsymbol{i}}(z_{i+1}^2 - z_i^2) \tag{3}$$

$$\boldsymbol{D} = \frac{1}{3}\sum_{i=1}^{n} \bar{\boldsymbol{Q}}_{\boldsymbol{i}}(z_{i+1}^3 - z_i^3) \tag{4}$$

where $\bar{\boldsymbol{Q}}_{\boldsymbol{i}}$ is the transversely isotropic stiffness matrix of a single ply containing information on the fiber orientation, and z_{i+1} and z_i are the locations of the upper and lower surfaces of the i-th ply. The mosaic model is used to account for the plain weave of the fabric [22], where the lamina stiffness matrices $\bar{\boldsymbol{Q}}_{\boldsymbol{i}}$ are computed by averaging the stiffness of warp, $\bar{\boldsymbol{Q}}_{\boldsymbol{i}}^{\boldsymbol{0^o}}$, and weft, $\bar{\boldsymbol{Q}}_{\boldsymbol{i}}^{\boldsymbol{90^o}}$, tows in the weave,

$$\bar{\boldsymbol{Q}}_{\boldsymbol{i}} = \frac{1}{2}\left(\bar{\boldsymbol{Q}}_{\boldsymbol{i}}^{\boldsymbol{0^o}} + \bar{\boldsymbol{Q}}_{\boldsymbol{i}}^{\boldsymbol{90^o}}\right) \tag{5}$$

Note that this model does not account for the effects of undulations in the fibers.

Following this method, the axial stiffness matrix, $\boldsymbol{A}$, in the local coordinate frame defined by the longitudinal axis 1 and the circumferential axis 2 in Figure 1A are given by,

$$\boldsymbol{A}_{\boldsymbol{e}} = \begin{bmatrix} 3696 & 1228 & 0 \\ 1228 & 3696 & 0 \\ 0 & 0 & 1332 \end{bmatrix} \text{ N/mm} \tag{6}$$

$$\boldsymbol{A}_{\boldsymbol{s}} = \begin{bmatrix} 1867 & 866 & 0 \\ 866 & 1867 & 0 \\ 0 & 0 & 860 \end{bmatrix} \text{ N/mm} \tag{7}$$

where the $\boldsymbol{e}$ and $\boldsymbol{s}$ subscripts denote AQ/epoxy and AQ/silicone composite properties, respectively.

It is known that the mosaic model can result in large inaccuracies in the bending stiffness, $\boldsymbol{D}$, particularly when applied to one- or two-ply laminates [22]. For low ply count composites, the undulations in the weave are on the same order of magnitude as the overall thickness of the laminate. The tows are hence subjected to both tensile and bending loads in response to an applied curvature, which has a significant impact on the bending stiffness. To improve the accuracy of the model, the stiffness coefficient in the axial direction of the hinge, $\boldsymbol{D}_{11}$, was measured experimentally using four-point bending tests of AQ/epoxy and AQ/silicone flat rectangular coupons. It was found that the mosaic model overpredicted the bending stiffness by 74% for the silicone composite and by 68% for the epoxy composite.

Furthermore, experimental studies of the bending of silicone reinforced laminates have shown a significant decrease in the bending stiffness when the laminates are bent to large curvatures, as a result of fiber microbuckling [16]. Here, it was found that the bending stiffness of the AQ/silicone composite at high curvatures is only 40% of the initial stiffness. As a result, the bending stiffness of the silicone composite in the circumferential direction of the hinge, $\boldsymbol{D}_{22}$, was reduced compared to that in the axial direction, $\boldsymbol{D}_{11}$, to account for the high curvature of the material in that direction (illustrated in Figure 1B).

The remaining coefficients of the bending stiffness matrices could not be measured experimentally. Their values were predicted by the mosaic model and scaled by $\boldsymbol{D}_{11,exp}/\boldsymbol{D}_{11,mm}$, where the $\boldsymbol{exp}$ and $\boldsymbol{mm}$ subscripts indicate measured values and Mosaic Model predictions, respectively. In conclusion, the bending stiffness for the two laminates that made up the hinge is given by,

$$\boldsymbol{D}_{\boldsymbol{e}} = \begin{bmatrix} 12.31 & 5.25 & 0 \\ 5.25 & 12.31 & 0 \\ 0 & 0 & 7.30 \end{bmatrix} \text{ N} \cdot \text{mm} \tag{8}$$

$$\boldsymbol{D}_{\boldsymbol{s}} = \begin{bmatrix} 3.61 & 1.35 & 0 \\ 1.34 & 1.45 & 0 \\ 0 & 0 & 2.46 \end{bmatrix} \text{ N} \cdot \text{mm} \tag{9}$$

Due to the symmetric layup of the composite, the stretch-bending coupling matrix, $\boldsymbol{B}$, is assumed to be zero.

3. Mechanics of Hinge Folding and Deployment

The parameters of interest are the natural radius of the localized fold and the deployment moment as a function of the folded angle. Prediction of these parameters allows for the design of deployment restraints and mechanisms.

3.1. Analytic Model

A simple model of two AQ/epoxy tape springs that are connected at the edges and are assumed to bend together is used to gain insight into the folding and deployment behavior of the dual-matrix hinge. A single tape-spring has the geometry in Figure 5A. The tape-spring can be folded either in equal- or opposite-sense bending, as illustrated in Figure 5B and C, respectively.

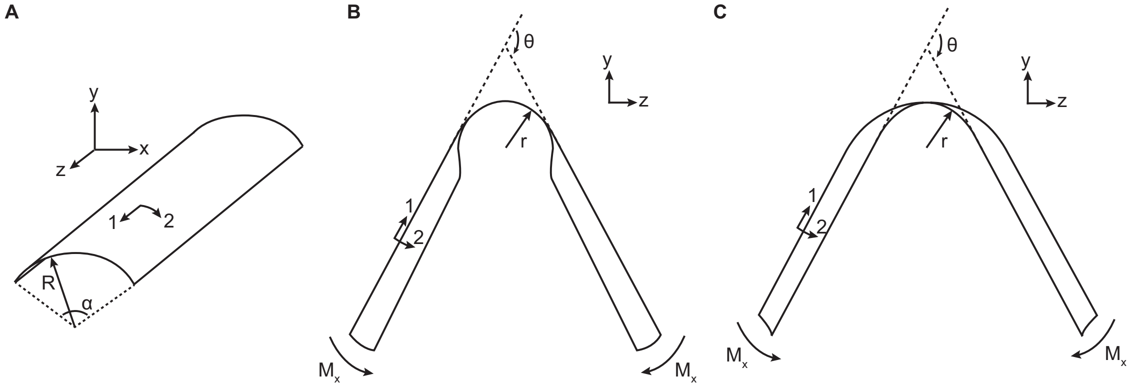

Figure 5: (A) single tape spring geometry (B) equal-sense bending (C) opposite-sense bending.

For small relative rotation angles, θ, the reaction moment, M_x, increases linearly until the tape spring buckles to form a localized fold. Past this angle, the tape-spring produces a constant reaction moment. The response is similar for both equal- and opposite-sense bending, but equal-sense bending results in lower reaction moments [23, 24]. This behavior is illustrated in Figure 6A, where the *es* and *os* subscripts indicate equal- and opposite- sense bending, respectively.

The mechanics of two connected tape-springs, one undergoing equal- and one opposite-sense bending, are analogous and can be predicted through superposition of the separate cases considered above. However, due to the connection between the two tape-springs, the folding angle of the outer tape spring is less than that of the inner tape spring during folding. Therefore, two distinct moment peaks are expected with the inner tape-spring buckling first upon folding. The response should be identical in either direction of folding of the hinge. This behavior is illustrated in Figure 6B.

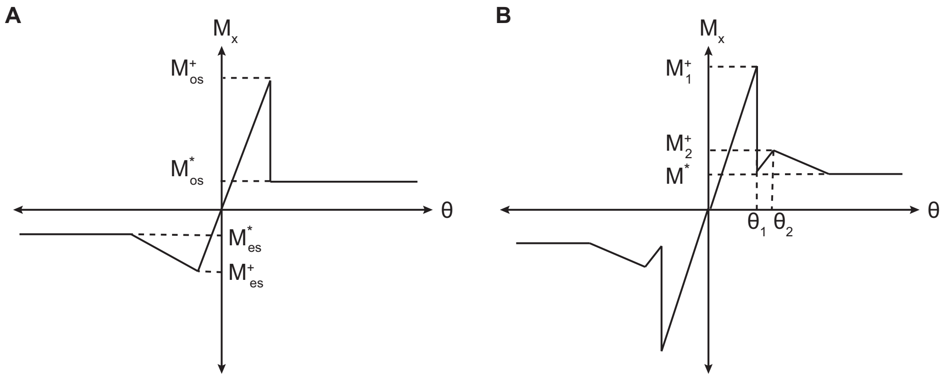

Figure 6: Predicted reaction moments (A) single tape-spring (B) combination of two tape-springs.

The mechanics of tape-springs can be analyzed using an energy approach as was done by Schulgasser [25] to obtain the natural fold radius of a single tape spring. Here, the analysis is extended to consider the energy contribution of the AQ/silicone strips. Only the bending energy in the fold region of the hinge is considered, as the energies in the transition regions are independent of the fold radius.

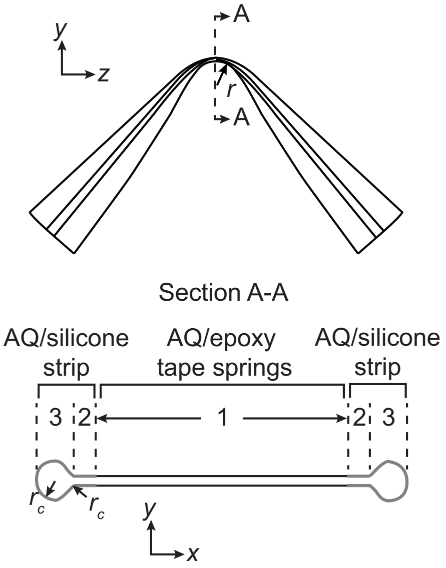

Figure 7: Cross-section of fold area of dual-matrix hinge.

The folded shape of the dual-matrix hinge has been sketched in Figure 7, with the cross-section at the fold region shown in the lower part of the figure. This cross-section can be divided into 3 regions: the flattened AQ/epoxy tape springs, the flattened portions of the AQ/silicone strips, and the approximately circular AQ/silicone connections at the end of radius r_c. In region 3, we assume that $r_c = 0.5t$ due to self-contact of the material, where t is the thickness of the material. Due to very high curvatures in the circumferential direction, the fibers microbuckle resulting in increased material thickness in region 3, forming a circular cross-section. We consider contributions to the bending strain energy from the deformation in regions 1 and

3. Region 2, as well as the transition between regions 2 and 3, are comparatively small and their contribution to the energy is neglected.

The AQ/epoxy tape-springs in region 1 undergo the following principal curvature changes,

$$[\boldsymbol{\kappa_e}]^T = [\Delta\kappa_{x,e}\ \Delta\kappa_{z,e}] = \left[\mp\frac{1}{r}\ \frac{1}{R}\right] \tag{10}$$

for opposite- and equal-sense bending respectively. The corresponding moments are given by,

$$[\boldsymbol{M_e}] = \begin{bmatrix} M_{x,e} \\ M_{z,e} \end{bmatrix} = \begin{bmatrix} D_{11,e}\kappa_{x,e} + D_{12,e}\kappa_{z,e} \\ D_{12,e}\kappa_{x,e} + D_{22,e}\kappa_{z,e} \end{bmatrix} \tag{11}$$

The total strain energy in the two AQ/epoxy tape-springs (region 1) is therefore,

$$U_1 = R\theta\alpha r[\boldsymbol{\kappa_e}]^T[\boldsymbol{M_e}] = \theta\alpha\left[\frac{RD_{11,e}}{r} + 2D_{12,e} + \frac{rD_{22,e}}{R}\right] \tag{12}$$

The AQ/silicone connections in region 3 undergo a large curvature change about the z-axis to form two cylindrical tubes of radius r_c connected to the edges of the AQ/epoxy tape-springs shown in Figure 7. Furthermore, these tubes are curved around the x-axis to form the dual-matrix hinge fold region of radius r. For bending around the z-axis, the energy can be computed from the curvature changes,

$$\Delta\kappa_{z,s} = \left(\frac{1}{r_c} - \frac{1}{R}\right) \tag{13}$$

The energy contribution from this deformation is,

$$U_{3,z} = 2\pi r_c r\theta D_{22,s}\left(\frac{1}{r_c} - \frac{1}{R}\right)^2 \tag{14}$$

The AQ/silicone cylindrical shell in region 3 undergoes the same curvature change along the x-axis as the AQ/epoxy tape-springs,

$$\Delta\kappa_{x,s} = \frac{1}{r} \tag{15}$$

The moment per unit length of the fold can be computed from,

$$M_{x,s} = \frac{12(1-\nu_s^2)\kappa I}{2\pi r_c t_s^3}D_{11,s} \tag{16}$$

where $I = \pi/4[(r_c + t_s)^4 - r_c^4]$ is the area moment of inertia for a hollow circular tube, t_s is the thickness of the AQ/silicone composite, and ν_s is the Poisson's ratio of the AQ/silicone composite. In computing the moments, the bending stiffness for a quasi-isotropic AQ/silicone composite plate is used.

Hence, the total energy contribution from bending of the circular tube is,

$$U_{3,x} = \frac{12(1-\nu_s^2)\theta I D_{11,s}}{rt_s^3} \tag{17}$$

Adding the three energy contributions in Equations 12, 14, and 17 and minimizing with respect to the fold radius, r,

$$r = \sqrt{\frac{R\alpha D_{11,e} + [12(1-\nu_s^2)I/t_s^3]D_{11,s}}{[\alpha/R]D_{22,e} + 2\pi r_c(1/r_c - 1/R)^2 D_{22,s}}} \tag{18}$$

This equation is valid only for $D_{11,s} = D_{22,s}$ due to the assumption of a quasi-isotropic AQ/silicone layup. The use of this equation when $D_{11,s} \neq D_{22,s}$, for example to account for fiber microbuckling, can only be used to predict trends in the fold radius.

There are several insights to draw from Equation 18. First, if the bending stiffness of the AQ/silicone strips tends to zero (i.e. no connection between the two tape-springs), we recover the fold radius expected for two tape springs given in [25],

$$r = \sqrt{\frac{D_{11,e}}{D_{22,e}}}R \tag{19}$$

For a quasi-isotropic tape-spring layup, where $D_{11,e} = D_{22,e}$, as for the AQ/epoxy composite used here, this simplifies to the well known result [25],

$$r = R \tag{20}$$

Hence, for quasi-isotropic unconnected tape-springs the fold shape is entirely controlled by the tape-spring geometry and is independent of material properties.

Second, if we assume the material properties of the AQ/epoxy tape-springs to be fixed, chosen on the basis of the overall required stiffness of the structure, it is predicted that the fold radius of the dual-matrix hinge can be controlled by modifying the bending stiffness of the AQ/silicone strips. Increasing the bending stiffness, $D_{11,s} = D_{22,s}$, decreases the fold radius. Reducing the circumferential bending stiffness to account for fiber microbuckling, will result in a larger fold radius compared to the quasi-isotropic case. This is of significance, as the fold radius of the dual-matrix hinge can be controlled even with a quasi-isotropic layup for both composites, which is not possible for two unconnected tape springs as indicated by Equation 20.

The steady-state moment, M^*, for the dual-matrix hinge can be obtained by substituting Equations 10 and 18 into the x-component of Equation 11. By superposition, M^* is the sum of moments from one tape-spring undergoing equal-sense bending and the other undergoing opposite-sense bending. The moments imparted by the AQ/silicone connection have a negligible contribution to M^*.

3.2. Quasi-static Deployment Experiments

The hinge deployment was characterized experimentally by measuring the quasi-static reaction moment for varying fold angles, θ, with the experimental setup in Figure 8. A small section at each end of the hinge was attached rigidly to a thick cylindrical hub whose rotation was controlled via gears. One hub was fixed while the other was allowed to slide on a linear bearing. The moment response was measured using strain gages attached to each hub. The hinge was pinched by hand at the center, folded to $\theta = 120^\circ$, and then deployed in small steps. The moment was measured every 5° for $40^\circ < \theta < 100^\circ$ and every 2° for $\theta < 40^\circ$ to capture the peak moments.

The dependence of the moment on the fold angle of the hinge is shown in Figure 9 for several slot widths, w_s. The experimental error stemming from the resolution of the strain gages is shown only for the case of $w_s = 40$ mm, for clarity. Qualitatively, the response for all w_s matches well the theoretical prediction illustrated in Figure 6B. Instead of the two distinct deployment peaks a broad region of increased moment for

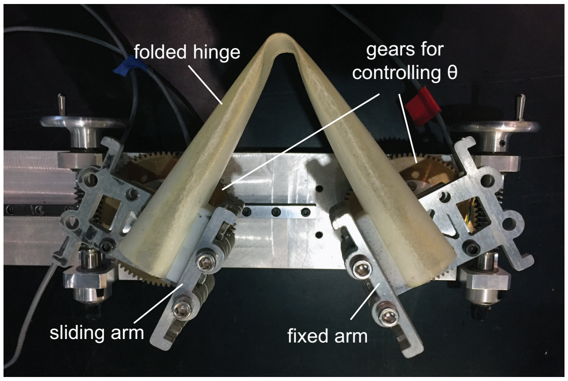

Figure 8: Experimental setup used to measure the moment response of the hinge during deployment.

$\theta < 40^{\circ}$ is observed. This is due to the tendency of the hinge to self deploy, making it difficult to capture the exact moment peak experimentally. Furthermore, $M_x > 0$ for all θ indicating that the hinge can self-deploy.

No correlation between the slot width and the deployment moments is observed. This can be expected as the deployment moment is driven mostly by the strain energy stored in the AQ/epoxy tape springs as the AQ/silicone strips are much softer and smaller in extent. The measured steady state moment, defined experimentally as the average moment for $40^{\circ} < \theta < 100^{\circ}$, is between 50–70 N·mm, a good agreement with $M^{*} = 63.7$ N·mm predicted using Equations 10, 11, and the experimentally predicted fold radius (shown in Figure 11). The 15% variation in peak moments between hinges with different slot lengths arises as it is difficult to maintain the hinge in its configuration just before snap back. Any remaining deviations in steady state moments are due to statistical variations in material properties and the fabrication process, as a similar variation was observed during testing of multiple samples with the same slot length.

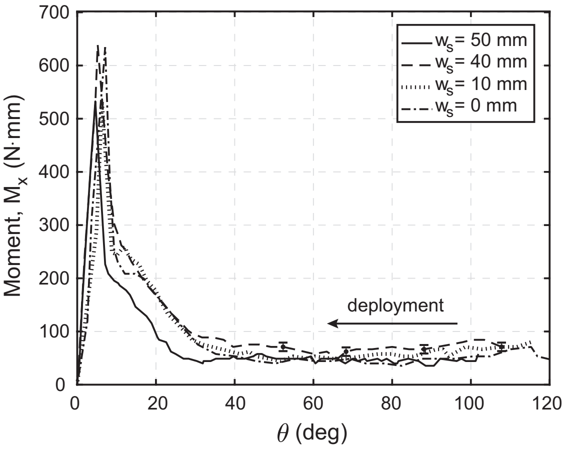

Figure 9: Experimentally measured moment response during deployment of hinges with various slot lengths.

To further characterize the deployment behavior, the folded shape was measured as a function of the fold angle using digital image correlation (DIC) for the hinge with $w_s = 0$ mm. The setup is illustrated in Figure 10. A pair of Grasshopper 50S5M-C cameras from Point-Grey Research with Xenoplan f/1.9-35 mm lenses from Schneider-Kreuznach were positioned 50 cm from the hinge to measure the shape of the fold region in the outer tape spring. The stereo angle was set at 40° to minimize the correlation error for a 35 mm lens [26]. A narrow f/16 aperture was used to achieve a focused image across all θ. The strains and curvatures during deployment were computed using the Vic3D software from Correlated Solutions.

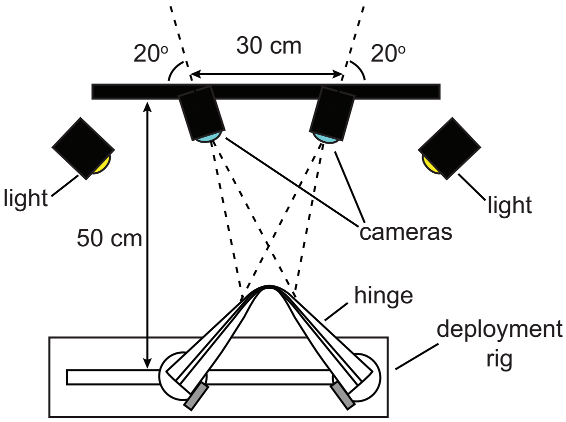

Figure 10: Experimental DIC setup for metrology of folded hinge shape.

Plots of the longitudinal radius of curvature at different fold angles are shown in Figure 11 for the hinge with $w_s = 0$ mm. The fold radius was computed by averaging the radius of curvature in a 12×5 mm^2 region centered on the apex of the fold (Figure 12). It can be seen that a steady-state fold radius of 10.0 mm is approached at high angles. As predicted by Equation 18, the addition of the silicone strips connecting the quasi-isotropic AQ/epoxy tape springs lowers the fold radius from that for two unconnected AQ/epoxy tape-springs of $r = 12.7$ mm (Equation 20). The effects of the AQ/silicone strip bending stiffness are further studied via finite element simulations in Section 5.2.

4. LS-Dyna Finite Element Simulations

The application of dual-matrix composites to space structures requires reliable and efficient simulation techniques for predicting the deployment behavior of these structures. In particular, quasi-static simulations can yield deployment moments to be used in the design of the deployment restraints for more complex structures. Previous studies have developed simulation techniques for deployable composite booms with an open cross-section [27, 28], booms with cutouts in the fold region to make localized hinges [29, 30], and booms with a fully closed cross-section [8, 31]. Explicit solvers have been used to avoid convergence issues associated with modeling large deformation in thin shells using shell elements, resulting in high computational costs to obtain quasi-static solutions. Solutions via implicit solvers for quasi-static deployment have been limited to boom geometries with large slots or open cross-sections.

Preliminary studies of the deployment of dual-matrix hinges were done using the Abaqus/Explicit finite element code in [31, 32]. However, a detailed investigation of the material properties of the dual-matrix composites was not done during those studies, resulting in large discrepancies between simulations and

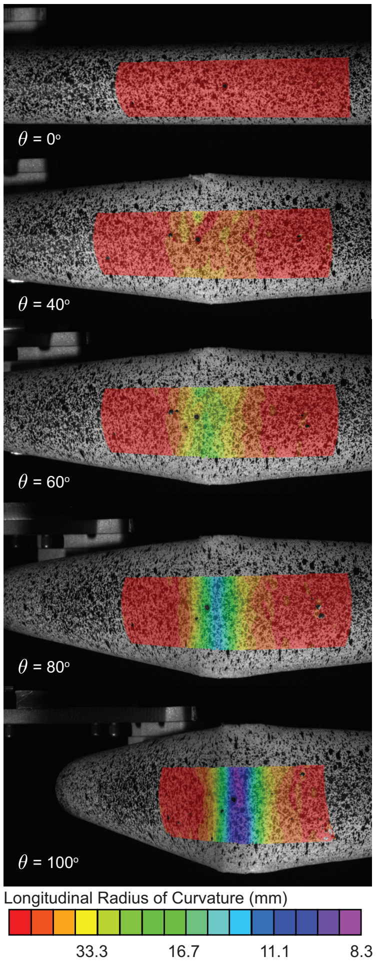

Figure 11: Longitudinal radius of curvature of outer tape-spring of dual-matrix hinge with w_s = 0 mm, for several deployment angles.

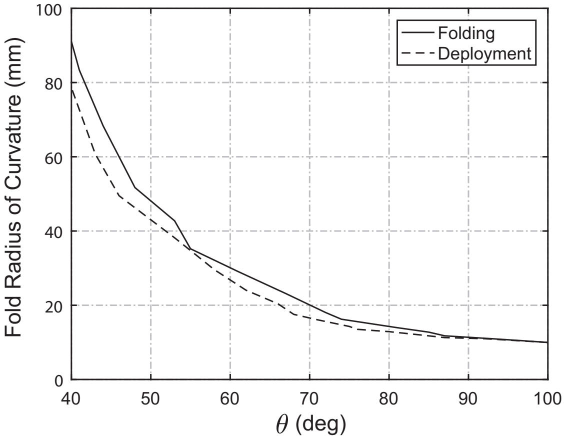

Figure 12: Longitudinal fold radius for dual-matrix hinge with w_s = 0 mm.

measurements. Previous work by the present authors found extreme sensitivity of the solution to numerical parameters such as damping, making it difficult to obtain accurate quasi-static results [32]. Furthermore, high frequency oscillations were observed in the reaction moments despite numerical damping and required filtering [31, 32].

In this study, LS-Dyna was chosen for modeling the deployment of the dual-matrix hinge because of its robust contact algorithms and good stability for highly non-linear problems. LS-Dyna is primarily an explicit finite element code; recently implicit analysis capabilities were extended to composite materials and thin shell elements. Explicit solvers are advantageous due to their ability to handle non-linearities, such as contact and material non-linearities, without convergence problems more easily than implicit solvers. However, care must be taken to ensure accuracy of the explicit results as equilibrium is not enforced at each step of the solution. Both explicit and implicit modeling techniques were investigated in the present study, as detailed in the rest of this section. The respective advantages of the two techniques are compared in Section 5.1.

4.1. Finite Element Model Description

The hinge was modeled with the type 16 shell element in LS-Dyna, a 4 node fully integrated element modeling the mid-plane of the material based on the Reissner-Mindlin kinematic assumption. The element size was 0.75 mm in the fold region and 3 mm in the rest of the model, resulting in approximately 15,000 elements. The stiffness of the two composite materials was defined via a linear elastic laminated plate material model, *`MAT_117-Composite_Matrix`, which allows direct input of the ABD matrix as specified in Section 2.3. This avoids inaccuracies associated with CLT when predicting out-of-plane stiffness of woven composite materials. Furthermore, this facilitates an investigation of the effect of the material properties of the hinge on the deployment. The material thickness and density were defined as measured in Section 2.3. Finally, frictionless contact between all surfaces in the simulation was defined using the keyword *`Contact_Automatic_Single_Surface`, a general 3D contact algorithm. This algorithm accounts for the thickness of the shell and uses a penalty formulation to enforce contact constraints. The model is shown in Figure 13.

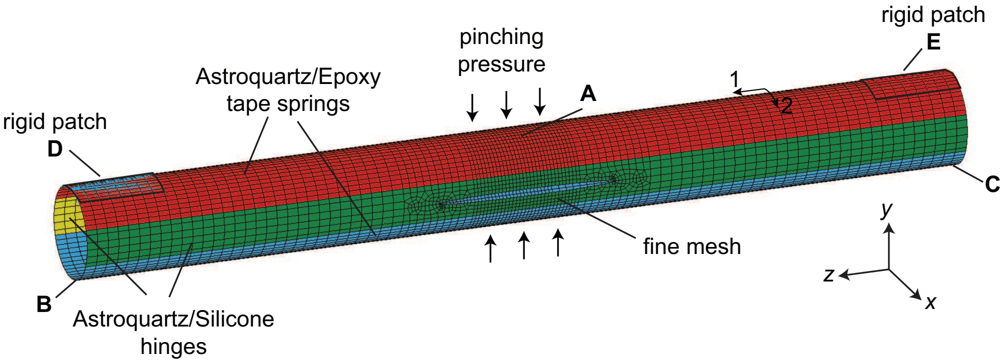

Figure 13: LS-Dyna model of the dual-matrix hinge.

The model included three steps: folding, stabilization, and deployment. To fold the hinge, a pressure of 12.5 Pa was applied in the fold area to pinch the shell, followed by opposing rotations of 1.5 rad applied to rigid patches at the two ends of the hinge with the pressure gradually removed. The rigid patches matched those in the experiments in Section 3.2, and are constrained using the keyword *`Constrained_Nodal_Rigid_Body`. The stabilization step, only required in the explicit model, was used to obtain a static, stable folded configuration. In the deployment step, the rotations at the rigid patches were reversed to slowly deploy the hinge.

4.2. Quasi-Static Simulations with an Explicit Solver

Explicit solvers use the full dynamic equations of motion and therefore, to carry out a quasi-static analysis, the applied velocities must be kept as low as possible. As a general heuristic, the kinetic energy is kept at $< 1\%$ of the internal energy for all parts of the simulation where a quasi-static result is required [30]. In this study, the kinetic energy in the system was controlled through the loading rates and numerical damping. More gradual loading rates and damping both result in lower velocities while damping also smooths instabilities. The selection of these two parameters influences the stable time increment used by the solver and hence directly impacts the overall computational time.

In LS-Dyna Explicit, two forms of numerical damping can be applied: global damping and bulk viscosity. Using global damping (*`Damping_Global` keyword), the accelerations at each node are computed by introducing a mass, m, and velocity, $\boldsymbol{v}$, proportional force to the force balance,

$$\boldsymbol{a} = \boldsymbol{M}^{-1}(\boldsymbol{F}^{ext} - \boldsymbol{F}^{int} - \boldsymbol{F}^{damp}) = \boldsymbol{M}^{-1}(\boldsymbol{F}^{ext} - \boldsymbol{F}^{int} - D_s m \boldsymbol{v}) \tag{21}$$

where $\boldsymbol{a}$ is the nodal acceleration, $\boldsymbol{M}$ is the mass matrix, $\boldsymbol{F}^{ext}$, $\boldsymbol{F}^{int}$ and $\boldsymbol{F}^{damp}$ are the external, internal, and damping force vectors, respectively, and $\boldsymbol{D_s}$ is the damping constant [33]. The LS-Dyna manual recommends a damping constant close to twice the natural frequency, ω_0, to damp out significant dynamic response at system resonance frequencies. In practice, the amount of damping should be as small as required to prevent a dynamic response. Large values of $\boldsymbol{D_s}$ will result in an over-damped response that is potentially inaccurate.

A second type of stabilization is achieved through bulk viscosity (*`Control_Bulk_Viscosity` keyword) where a viscous pressure term, q, is added to smooth out discontinuities,

$$q = \begin{cases} \rho l (Q_1 l \dot{\varepsilon}_{kk}^2 - Q_2 a \dot{\varepsilon}_{kk}) & \dot{\varepsilon}_{kk} < 0 \\ 0 & \dot{\varepsilon}_{kk} \geq 0 \end{cases} \tag{22}$$

where Q_1 and Q_2 are the quadratic and linear bulk viscosity coefficients, $\dot{\varepsilon}_{kk}$ is the rate of change of the volumetric strain, l is the characteristic length of the element, and a is the speed of sound [33].

The magnitude of numerical damping will influence the stable time increment for the simulation. The Courant stability condition indicates that in explicit analysis the time step should not exceed the time it takes for a wave to travel across an element,

$$\Delta t_{crit} = \frac{l}{c} \left(\sqrt{1 + \zeta^2} - \zeta \right) \tag{23}$$

where c is the wave speed, and $\zeta = D_s/(2m\omega)$ is the fraction of critical damping [33]. It can be seen that increasing damping will reduce the stable time increment.

4.3. Explicit Model Parameter Selection

Simulation phase	Viscous damping D_s (rad/s)	Time period (s)	Boundary Conditions				
			A	**B**	**C**	**D**	**E**
Folding	5	0.6	$u_x = u_y = u_z = 0$	$u_x = 0$	$u_x = 0$	$\theta_x = -1.5$ rad	$\theta_x = 1.5$ rad
Stabilization	75	0.25	$u_x = 0$	none	none	$u_x = u_y = u_z = 0$ $d\theta_x/dt = 0$	$u_x = u_y = 0$ $d\theta_x/dt = 0$
Deployment	50	4	$u_x = 0$	none	none	$u_x = u_y = u_z = 0$ $d\theta_x/dt = 1.5$ rad	$u_x = u_y = 0$ $d\theta_x/dt = -1.5$ rad

Table 4: Simulation parameters for explicit model.

The explicit model consisted of the folding, stabilization, and deployment steps with full restarts between each simulation step. The restarts were required as the boundary conditions to obtain the folded shape were selected to minimize numerical damping and hence reduce the computation times but do not match those of the deployment experiments in Section 3.2. The model boundary conditions and parameters are summarized in Table 4, where the boundary condition regions correspond to those defined in Figure 13.

Global mass damping and bulk viscosity are used to stabilize all steps of the simulation. The fundamental frequency of vibration of the hinge is 1281 rad/s and hence the recommended damping constant is $D_s = 2562$ rad/s. However, in practice it was found that this value is orders of magnitude too high, a common trend when running quasi-static simulations using explicit dynamics [30]. The damping values were chosen such that the response of the hinge is critically damped and the kinetic energy during deployment is $< 1\%$ of the internal energy. Furthermore, the time step chosen for explicit analysis was set at $dt = 7.9 \times 10^{-8}$ s to satisfy the Courant condition.

4.4. Implicit Model Parameter Selection

Implicit models solve the static force balance by inversion of the stiffness matrix and hence they satisfy equilibrium at each increment. Instabilities and contact can cause singularities in the stiffness matrix and make convergence difficult. There is no numerical damping required in these simulations, although artificial stabilization can be used to improve convergence [33]. No stabilization was required for this model. The stable increment in implicit analysis is several orders of magnitude larger than in explicit analysis and is often limited by the contact algorithm.

The boundary conditions of the implicit model were identical to those of the deployment step (and experiments) in Table 4. No restarts were required and the hinge was folded and deployed in a single analysis step. Static implicit analysis was enabled by including the *`Control_Implicit_General` keyword. Non-linear analysis is used to account for geometric non-linearities. The folding and deployment was done over 4.85 s with the increment set to $dt = 5.0\times10^{-5}$ s, allowed to vary automatically between $dt/1000 < dt < 10dt$. This increment was found to be the maximum for which convergence could be achieved. Note that the times here have no physical significance and are instead representative of the load increments used in the simulation.

Contact in implicit analysis in LS-Dyna is by default 'sticky' i.e. once contact has occurred, a large penalty is applied to keep the parts in contact. This prevents the parts from coming in and out of contact and causing instabilities in the analysis. This behavior is controlled by the `IGAP` parameter of the contact algorithm and can be turned off by changing the parameter from 1 to 2 to disable the contact penalty. Alternatively, the `SFS` parameter can be modified to scale the penalty.

The contact parameters were tuned to compute an accurate folded shape for the hinge. With the default 'sticky' contact, the two tape springs remained in contact and would not deploy, resulting in an inversion in the sign of longitudinal curvature in the outer tape spring (Figure 14A). Selecting `IGAP` = 2 to disable the contact penalty resulted in contact constraint violations at the tape spring edges unless the time increment was significantly reduced (Figure 14B). To enable larger increments, the `SFS` parameter was scaled down to `SFS` = 0.01, reducing the contact penalty to 1% of its original value. This setup prevented contact failure while allowing larger time increments and reducing 'sticky' contact enough to allow tape spring deployment (Figure 14C).

5. Finite Element Results and Discussion

5.1. Comparison of Models

A notable difference between the explicit and implicit models is the value of the stable increment used in the simulations. The explicit model had an increment of $dt = 7.9\times10^{-8}$ s whereas the implicit model had an average increment of $dt = 5.0\times10^{-5}$ s, three orders of magnitude larger. This resulted in a large difference in the runtime of the models. Despite using restarts to speed up explicit analysis, the three analysis steps needed to fold and deploy the hinge with w_s = 50 mm with an explicit solver took 35.17 hours on 8 cores (Intel Xeon X5680 CPU) whereas the implicit solver took only 1.01 hours on 8 cores.

Moreover, a difference in the resulting folded shape was observed between the two models. It was found that the explicit model produced the smooth folded shapes observed experimentally, whereas the implicit model produced sharp kinks in the AQ/silicone connections (Figure 15). This effect was localized to a small portion of the AQ/silicone connections and had small effects on the fold radius. The deployment moments predicted by the two models agreed well despite the differences in folded shape.

Previous attempts by the authors to model this problem with the Abaqus/Explicit code revealed strong dependence of the simulation results with numerical damping [32]. The explicit model here was significantly more stable and required less tuning of the damping parameters. No filtering of the reaction moments

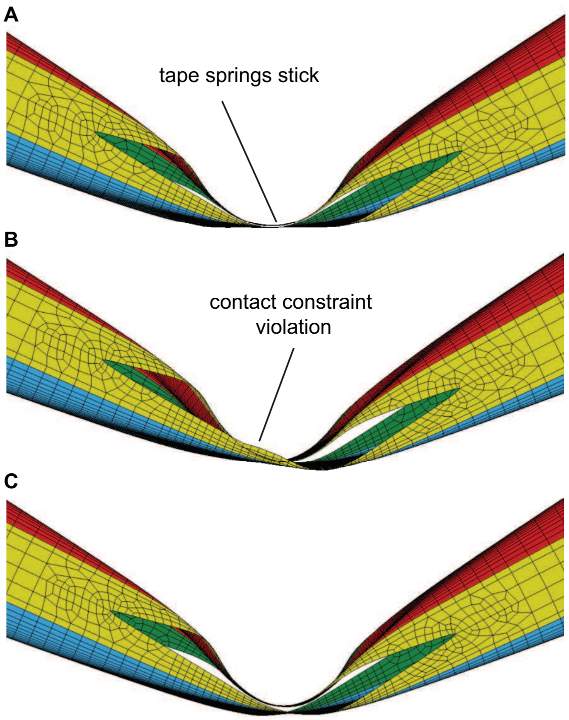

Figure 14: Effects of contact penalty on deployed shape at $\theta = 60^o$ of the hinge with $w_s = 50$ mm (A) LS-Dyna defaults - 'sticky' contact (B) `IGAP` = 2 – 'sticky' contact disabled (C) `SPS` = 0.01 – contact penalty reduced to 1%.

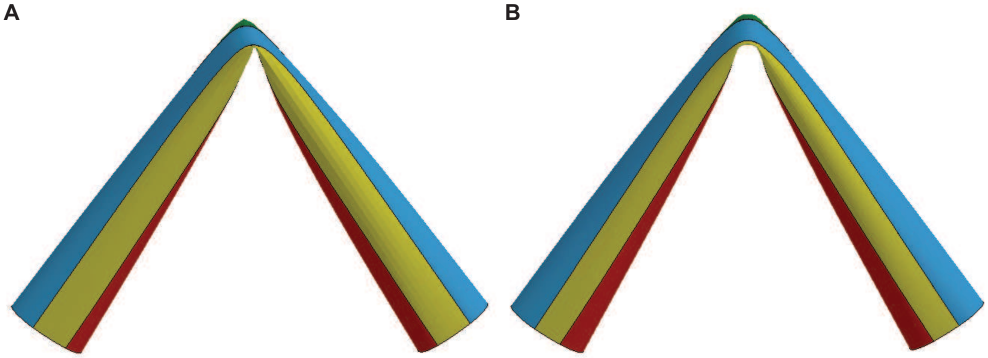

Figure 15: Comparison of folded shape (A) Implicit model (B) Explicit model.

was required to remove high-frequency oscillations. Convergence using implicit solvers in Abaqus was not successful for this problem, but it was achieved without stabilization in the LS-Dyna simulations.

5.2. Folded Hinge Shape

From the analytical prediction with Equation 18, it is expected that, for fixed AQ/epoxy material properties, the bending stiffness of the AQ/silicone strips will have a significant impact on the overall fold radius of the dual-matrix hinge, r. Hence, an investigation was conducted on the hinge with $w_s = 0$ mm where the bending stiffness of the AQ/silicone composite was varied through numerical simulations. Figure 16A illustrates the resulting steady-state fold radii, simulated using the explicit solver, for several values of the stiffness, assuming a quasi-isotropic layup where $D_{11,s} = D_{22,s}$. The explicit simulations show good agreement with the analytical predictions (using $r_c = 0.57$ mm for the radius of the AQ/silicone tubes formed during transverse flattening of the hinge). It can be seen that reducing the bending stiffness of the connection between the tape springs increases the fold radius of the hinge. This demonstrates that the AQ/silicone connections can be used to tune the fold radius even for quasi-isotropic layups for both composites, as predicted in Section 3.1.

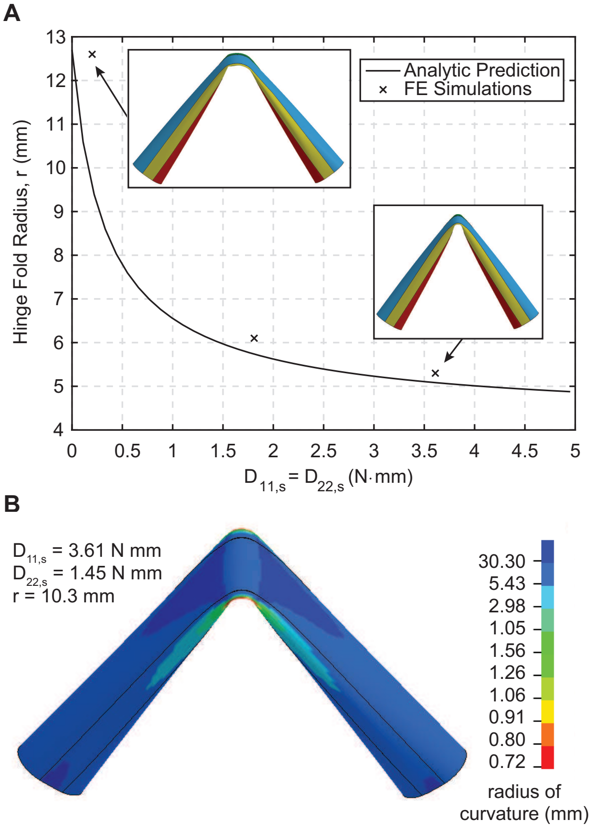

Figure 16: Comparison of analytic prediction of dual-matrix hinge fold radius and explicit simulations (A) Dependence on silicone composite bending stiffness (B) Predicted folded shape using measured silicone composite bending stiffness; contour shows the longitudinal radius of curvature.

In Figure 16B, the bending stiffness matches the experimental values where $D_{22,s} = 1.45$ N·mm is reduced to 40% of $D_{11,s} = 3.61$ N·mm to account for microbuckling of the fibers, as discussed in Section 2.3. In this case, the fold radius of 10.3 mm obtained through simulation is in excellent agreement with the value $r = 10.0$ mm measured experimentally (3% error). Applying the model in Equation 18, a fold radius of $r = 6.7$ mm is predicted for the case of $D_{11,s} \neq D_{22,s}$. Comparing this value to the $r = 5.0$ mm prediction for the quasi-isotropic case $D_{11,s} = D_{22,s} = 3.61$ N·mm, it can be seen that the model predicts the increase in fold radius due to microbuckling observed experimentally. However, the model results in an 33% error from the experimental value of $r = 10.0$ mm. This is to be expected as the model assumes quasi-isotropic properties.

5.3. Deployment Moments

Figure 17 shows the deployment moments for implicit and explicit simulations compared to experimental results for the hinge with $w_s = 40$ mm. Furthermore, Table 5 summarizes key deployment moment values for the three cases. Both implicit and explicit solvers predict the experimental behavior well, with the steady state moments within experimental error. The simulations show two distinct peaks corresponding to the deployment of the two tape springs as predicted in Figure 6B in Section 3.1. The peak moments predicted in simulation are larger than measured. Experimentally, the hinge tends to self deploy and hence a lower peak moment is measured. Furthermore, the significant difference between peak moments from the two simulations is due to the smaller time step, and hence finer load increments, of the explicit simulation allowing it to provide a finer angular resolution.

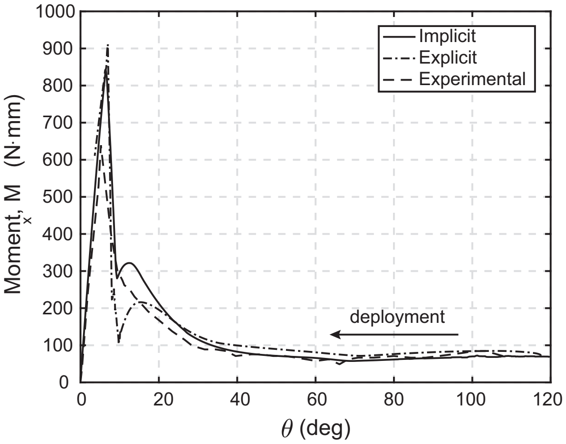

Figure 17: Comparison of finite element simulation and experimental results for a hinge with a 40 mm slot.

	Implicit Solver	**Explicit Solver**	**Measurement**
M^* **(N·mm)**	67	75	69
M_1^+ **(N·mm)**	843	910	639
θ_1 **(deg)**	6.4	7.0	5.2

Table 5: Summary of key values of deployment response of hinge with $w_s = 40$ mm.

Figure 18 shows the dependence of the deployment moment on w_s in the implicit simulations. The same trend is seen for the explicit simulations. A comparison with Figure 9 reveals that the simulations predict a much higher dependence of the moment on the slot length than is observed experimentally. Reducing the mesh size in the fold region, or reducing the transverse bending stiffness of the silicone composite, D_{22}, does not resolve the discrepancy. The higher moments seen in simulation are attributed to the fully integrated elements used being too stiff when doubly curved. An investigation of the dependence on element type is beyond the scope of the present study. Since experimentally there is little dependence on w_s, the model with w_s = 40 mm can be used to predict the deployment moments of hinges without slots. This is the model with the smallest slot which removes the effects of doubly curved elements from the results.

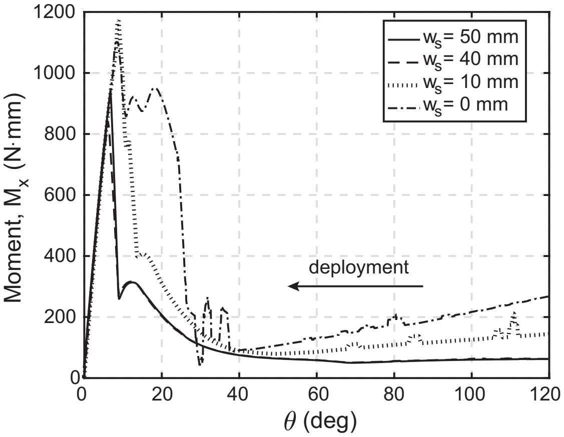

Figure 18: Dependence of deployment moment on the slot length in simulation - implicit model.

5.4. Torsional Behavior

The closed cross-section of the dual-matrix hinges can provide superior torsional behavior compared to open cross-section booms such as the TRAC and STEM booms. However, the introduction of small slots in the AQ/silicone fold region, to remove the doubly-curved region and alleviate stresses, can have a significant effect on the torsional stiffness. The torsional behavior of the hinge was simulated in LS-Dyna implicit with the Ricks and Wempner arc-length method to capture the post-buckling response. The same hinge model as for folding was used. The hinge was clamped at one end and a rotation, ϕ, was applied around the z-axis of the hinge at the other.

Figure 19 shows the dependence of the torsional stiffness on w_s, where G is the shear modulus and J is the torsion constant. It can be seen that introducing small slots has a negligible effect, with w_s = 10 mm reducing the torsional stiffness by only 8%. However, for longer slots the torsional stiffness decreases more quickly. Hence, introducing a small 10 mm slot is a good way of alleviating stresses in dual-matrix hinges while maintaining their superior torsional behavior.

6. Conclusion

Dual-matrix composite shells have been proposed as a means of realizing stiff, lightweight structures capable of accommodating packaging schemes with small fold radii through the use of localized elastomer composite hinges. Previous research has focused on the elastomer composite constitutive modeling or on proof-of-concept studies of folding of dual-matrix structures. This paper presented a more detailed look at

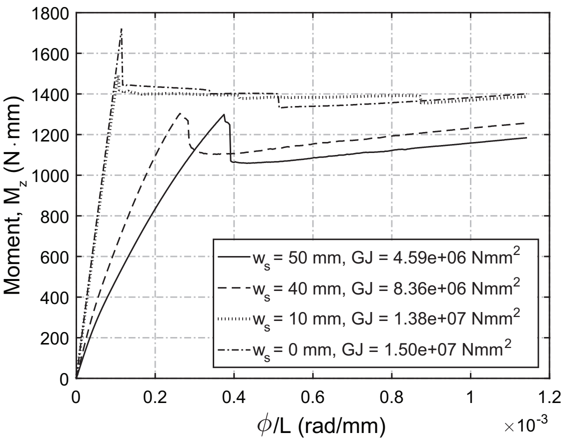

Figure 19: Simulated torsional stiffness of hinges with various slot widths.

the deployment mechanics of a simple closed cross-section dual-matrix hinge which can be used as a building block for more complex deployable structures. The proposed hinge can be used to stow instruments for launch to be deployed from a spacecraft once on orbit. In addition, the hinge building block can be extended to construct deployable space structures such as booms, space frames, and large area thin shells including antennas, solar panels, and telescope support structures. Furthermore, terrestrial applications requiring lightweight, self-deployable structures with multiple stowage and deployment cycles can benefit from this work, including portable communications antennas, and support structures for tents.

This study focused on characterizing the quasi-static deployment behavior of the proposed building block in terms of its folded shape and deployment moments. These parameters are critical to the design of deployment mechanisms for dual-matrix structures. The hinge was studied using an analytic minimum energy approach, experimental deployment tests, and finite element simulations – with good agreement between all models. The radii of the localized fold in the hinge could be predicted within 3% of experimental measurements while the steady-state reaction moments of the hinge could be predicted within 5% of measurements. This suite of analysis tools can be used to investigate the engineering applications described above.

In addition to the development of analysis techniques for deployment of dual-matrix shells, this work also identified several interesting aspects of the behavior of these composites. As these structures rely on stored strain energy for deployment, the importance of using accurate material properties was demonstrated. In particular, the bending stiffness of the shells has a large impact on deployment moments and folded shape. It was found that the transverse bending stiffness of the elastomer composite must be reduced by as much as 60% to experimentally measured stiffnesses at high laminate curvatures to account for fiber microbuckling. Furthermore, the use of the elastomer composites to tailor the fold radius of the hinge was demonstrated, a behavior not possible with simple quasi-isotropic tape springs. It was shown that the addition of elastomer hinges reduces the localized fold radius from that of unconnected tape-springs. This shows the versatility of the hinge building block to meet various packaging requirements independent of the overall stiffness of the structure. Finally, techniques for simulation of this deployment problem using the LS-Dyna commercial software were developed, taking advantage of the robust restart capabilities and the stabilization of the contact algorithms to improve computational times. The implicit solver showed a reduction in run times by a factor of 30 over the more commonly used explicit solver.

Although the finite element simulation techniques presented here proved very accurate for predicting the deployment moment for dual-matrix hinges with small slots, issues with the shell elements were highlighted when used for simulating doubly curved regions. A study of element types appropriate for high Gaussian curvatures is suggested as a follow-on study to this work. Of particular interest is the application of continuum shells with thickness stretch and multiple through-thickness integration points to this problem.

Acknowledgments

Financial support for this work was provided by the Air Force Office of Scientific Research award no. FA9550-13-1-0061.

Data Availability

The raw and processed data required to reproduce these findings are available to download from `dx.doi.org/10.17632/zkpj2b22fg.1`.

References

[1] M. W. Thomson, The AstroMesh deployable reflector, in: IEEE Antennas and Propagation Society International Symposium: Wireless Technologies and Information Networks, APS 1999 - Held in conjunction with USNC/URSI National Radio Science Meeting, Vol. 3, 1999, pp. 1516–1519. `doi:10.1109/APS.1999.838231`.

[2] C. Clark, S. Kirk, Off-the-Shelf, Deployable Solar Panels for CubeSats (2012).
URL `http://mstl.atl.calpoly.edu/~bklofas/Presentations/DevelopersWorkshop2012/Clark_Solar_Panels.pdf`

[3] M. Clampin, JWST Observatory Status, in: Joint APS-SCCM / AIRAPT Conference, 2013.

[4] F. Rimrott, Storable Tubular Extendible Member: a Unique Machine Element, Journal of Machine Design 37 (1965) 156–165.

[5] Northrop Grumman, STEM Products and Programs (2012).
URL `http://www.northropgrumman.com/BusinessVentures/AstroAerospace/Products/Documents/pageDocs/STEM_Hardware_Programs.pdf`

[6] J. A. Banik, T. W. Murphey, Performance Validation of the Triangular Rollable and Collapsible Mast, in: 24th Annual AIAAUSU Conference on Small Satellites, Logan, Utah, 2010.

[7] M. Aguirre, A. Bureo, M. Fuentes, J. Rivacoba, The Collapsible Tube Mast (CTM), in: Proceedings of the Second European Space Mechanisms and Tribology Sysmposium, 9-11 Oct. 1985, Meersburg, Germany, pp. 75–81.

[8] C. Sickinger, L. Herbeck, T. Strohlein, J. Torrez-Torres, Lightweight Deployable Booms: Design, Manufacture, Verification, and Smart Materials Application, in: 55th International Astronautical Congress of the International Astronautical Federation, the International Academy of Astronautics, and the International Institute of Space Law, Vancouver, Canada, 2004. `doi:10.2514/6.IAC-04-I.4.10`.

[9] L. Datashvili, H. Baier, E. Wehrle, T. Kuhn, J. Hoffmann, Large Shell-Membrane Space Reflectors, in: 51st AIAA/ASME/ASCE/AHS/ASC Structures, Structual Dynamics, and Materials Conference, Orlando, Florida, 2010. `doi:10.2514/6.2010-2504`.

[10] L. D. Peel, J. Mejia, B. Narvaez, K. Thompson, M. Lingala, Morphing Wing Using Elastomeric Composites as Skins, Journal of Mechanical Design 131. `doi:10.1115/1.3159043`.

[11] I. Maqueda, S. Pellegrino, J. Mejia-Ariza, Characterization of a High Strain Composite Material, in: 53rd AIAA/ASME/ASCE/AHS/ASC Structures, Structural Dynamics and Materials Conference, 23-26 April 2012, Honolulu, Hawaii, 2012.

[12] K. Saito, S. Pellegrino, T. Nojima, Manufacture of Arbitrary Cross-Section Composite Honeycomb Cores Based on Origami Techniques, Journal of Mechanical Design 136 (5) (2014) 1–9. `doi:10.1115/1.4026824`.

[13] J. Costantine, Y. Tawk, I. Maqueda, M. Sakovsky, G. Olson, S. Pellegrino, C. G. Christodoulou, Deployable Helical Antennas for CubeSats, IEEE Transactions on Antennas and Propagation 64 (9) (2016) 3752–3759. `doi:10.2514/6.2013-1671`.

[14] W. H. Francis, M. S. Lake, J. S. Mayes, A review of classical fiber microbuckling analytical solutions for use with elastic memory composites, in: 47th AIAA/ASME/ASCE/AHS/ASC Structures, Structural Dynamics, and Materials Conference, 1 - 4 May 2006, Newport, Rhode Island, Newport, Rhode Island. `doi:10.2514/6.2006-1764`.

[15] T. W. Murphey, T. Meink, M. M. Mikulas, Some micromechanics considerations of the folding of rigidizable composite materials, in: 42nd AIAA/ASME/ASCE/AHS/ASC Structures, Structural Dynamics, and Materials Confernece, 16-19 April 2001, Seattle, WA. `doi:10.2514/6.2001-1418`.
URL `http://arc.aiaa.org/doi/10.2514/6.2001-1418`

[16] I. Maqueda, High-strain composites and dual-matrix composite structures, Ph.D. thesis, California Institute of Technology (2014).

[17] F. López Jiménez, S. Pellegrino, Constitutive modeling of fiber composites with a soft hyperelastic matrix, International Journal of Solids and Structures 49 (2012) 635–647. `doi:10.1016/j.ijsolstr.2011.11.006`.

[18] J. C. Materials, JPS Databook, Tech. rep. (2015).
URL `http://jpsglass.net/wp-content/uploads/2015/08/docslide.us_jpsdatabook-55845c9747baf.pdf`

[19] Henkel, Loctite 5055 Technical Data Sheet, Tech. rep. (2010).
URL `http://www.loctite.com.au/aue/content_data/283350_5055EN.pdf`

[20] Patz Materials and Technologies, Current PMT Prepreg Resin Systems (2018).
URL `http://patzmandt.com/services/`

[21] I. M. Daniel, O. Ishai, Engineering Mechanics of Composite Materials, 2nd Edition, Oxford University Press, 2005.

[22] Ö. Soykasap, Micromechanical Models for Bending Behavior of Woven Composites, Journal of Spacecraft and Rockets 43 (5) (2006) 1093–1100. `doi:10.2514/1.18010`.

[23] K. A. Seffen, S. Pellegrino, Deployment dynamics of tape springs, Proceedings of the Royal Society A: Mathematical, Physical and Engineering Sciences 455 (1983) (1999) 1003–1048. `doi:10.1098/rspa.1999.0347`.

[24] S. Pellegrino, Folding and Deployment of Thin Shell Structures, in: D. Bigoni (Ed.), Extremely Deformable Structures, Springer, Vienna, 2015, pp. 179–267. `doi:10.1007/978-3-7091-1877-1_5`.

[25] K. Schulgasser, Configuration of a bent tape of curved cross-section, Transactions of the ASME, Journal of Applied Mechanics 59 (1992) 692–693.

[26] P. Reu, Stereo-rig design: Stereo-angle selection - Part 4, Experimental Techniques 37 (2) (2013) 1–2. `doi:10.1111/ext.12006`.

[27] C. Leclerc, L. Wilson, M. Bessa, S. Pellegrino, Characterization of ultra-thin composite triangular rollable and collapsible booms, in: 4th AIAA Spacecraft Structures Conference, Grapevine, Texas. (AIAA 2017-0172), 2017.

[28] A. Stabile, S. Laurenzi, Coiling dynamic analysis of thin-walled composite deployable boom, Composite Structures 113 (1) (2014) 429–436. `doi:10.1016/j.compstruct.2014.03.043`.

[29] Ö. Soykasap, Deployment analysis of a self-deployable composite boom, Composite Structures 89 (3) (2009) 374–381. `doi:10.1016/j.compstruct.2008.08.012`.

[30] H. Mallikarachchi, S. Pellegrino, Quasi-Static Folding and Deployment of Ultrathin Composite Tape-Spring Hinges, Journal of Spacecraft and Rockets 48 (1) (2011) 187–198. `doi:10.2514/1.47321`.

[31] K. Ubamanyu, H. Mallikarachchi, Simulation of Dual-Matrix Composite Boom, in: Proceedings of Annual Session of Society of Structural Engineers, 2016.

[32] M. Sakovsky, S. Pellegrino, H. Mallikarachchi, Folding and Deployment of Closed Cross-Section Dual-Matrix Composite Booms, in: 3rd AIAA Spacecraft Structures Conference, San Diego, CA. (AIAA 2016-0970), 2016.

[33] Livermore Software Technology Corporation, LS-Dyna Keyword User's Manual, Tech. rep. (2012).